

# Flow dynamics of a pulsed planar expansion

Ludovic Biennier<sup>a,\*</sup>, Abdessamad Benidar<sup>a</sup>, Farid Salama<sup>b</sup>

<sup>a</sup> *Laboratoire de Physique des Atomes, Lasers, Molécules et Surfaces, Université Rennes 1, Rennes, France*

<sup>b</sup> *Space Science Division – NASA Ames Research Center, Moffett Field, 94035-1000 CA, USA*

Received 15 September 2005; accepted 3 March 2006

Available online 20 March 2006

## Abstract

Plasma expansion sources are popular in molecular spectroscopy and in astrochemistry because they generate cold radicals and ions in detectable amounts. The dynamics of a planar flow generated by a pulsed discharge slit nozzle (PDN) have been numerically investigated for a variety of carrier gases seeded with various molecular species. The determination of the bulk flow characteristics is key to a comprehensive modeling of the plasma that is produced in PDN sources. It is found that the flow is established and stabilized within 75 and 25  $\mu\text{s}$  when Ar and He are used as carrier gases, respectively. The residence time in the inter-electrode active region is found to be considerably shorter with He than with Ar gas carrier. The detection signal observed upon injection of astrochemical species such as polycyclic aromatic hydrocarbons (PAHs) in moderate amounts in the carrier gas exhibits a non linear relation with the initial PAH concentration in the reservoir which is governed by the temperature. The local temperature along the flow axis can be predicted from the initial conditions using the isentropic equation. However, the local pressure and density behavior diverge significantly from an isentropic flow. Finally, implications for the characteristics of the plasma expansion are discussed to help design future laboratory simulations.

© 2006 Elsevier B.V. All rights reserved.

**Keywords:** Computational flow dynamics; Pulsed planar expansions; Pulsed discharge nozzles; Astrochemistry; Molecular spectroscopy; Polycyclic aromatic hydrocarbons

## 1. Introduction

Interstellar carbon species are involved in many fundamental processes that take place in environments highly diverse ranging from circumstellar envelopes of carbon rich evolved stars to the core of dense interstellar clouds to the diffuse interstellar medium [1]. Polycyclic aromatic hydrocarbons (PAHs) are considered to be an important component of interstellar carbonaceous dust. PAH molecules and ions are thought to account for two unexplained ubiquitous observations that have been challenging the astronomical community for decades: namely, the unidentified infrared emission bands (UIBs) [2,3] and the diffuse interstellar absorption bands (DIBs) seen in the visible and near

infrared absorption spectra of diffuse interstellar clouds [4]. Little is known, however, of the properties of these complex carbon molecules in interstellar environments where low temperature and collision-free conditions dominate. An extensive laboratory research program has been dedicated for the past decade to the study of these species under laboratory conditions that are relevant to space studies (for a review see Ref. [5]). The formation and the study of interstellar PAH analogues in the laboratory are essential for an unambiguous identification of specific PAH species in space and to quantify the astrophysical models that describe the evolution of interstellar clouds.

Supersonic plasma sources have opened new possibilities to attain this objective by allowing the generation of astrochemical species in the laboratory. They have been intensively used to produce isolated gas-phase carbon chains [6], which are cooled down and stabilized in the supersonic expansion, thus facilitating mass or optical

\* Corresponding author. Tel.: +33 2 23 23 61 90; fax: +33 2 23 23 67 86.  
E-mail address: [ludovic.biennier@univ-rennes1.fr](mailto:ludovic.biennier@univ-rennes1.fr) (L. Biennier).

detection (i.e. in the sub-ppm range) [7]. The expansion of their utilization is intimately linked to the development of high resolution and sensitivity spectroscopic techniques now capable to probe species generated in the plasma even in modest number densities in the microwave and optical regions. Sources with long-slit orifices have proven to be efficient in obtaining high column densities of molecular ions and free radicals [8,9]. Recently, supersonic planar plasma sources have been developed to generate cold PAH cations in the gas phase, and, when combined with Cavity Ring Down spectrometers, to measure their optical absorption spectra [10–13]. This approach complements other laser-based sophisticated methods such as photo-depletion [14,15]. The ultimate objective of these investigations is to assess the spectral contribution of PAHs to the diffuse interstellar bands seen in absorption in line of sights crossing diffuse interstellar clouds.

In the prospect of optimizing the yield of PAH ions formed in the PDN source and more generally molecular ions and free radicals, and to correctly assess the relevance of the ion formation setting in the laboratory to astrophysical environments, the nature of the plasma environment in which the species are generated was investigated [16]. These experimental measurements were mostly based on the study of the post discharge region and the plasma current–voltage characteristics.

To gain a better understanding of the processes that take place in the plasma, we have now turned our attention to a detailed quantitative modeling of the plasma, which is described, in a separate paper [17,18]. Since the power dissipated in the discharge is low enough (<50 W) to not cause appreciable gas heating, the flow of the background gas can be described *independently* from the plasma which is weakly ionized. The only region where the flow may be slightly affected by the plasma is the area very close to the cathode tip. In this very small region characterized by a strong electric field, ions that are present in high density gain more energy from the electric field than they lose by collisions. But overall, one can *reasonably* use the calculated flow velocity, temperature and density fields in absence of discharge as fixed input values for modelling the plasma characteristics. The accurate determination of the flow physical conditions that reign in the plasma region has motivated the present investigation.

A limited number of studies dealing with continuous supersonic expansions produced by slit jet sources has been performed (see, e.g. Ref. [19]), but to the best of our knowledge, there is no detailed numerical description of the dynamics of pulsed planar expansions in the literature that could be directly applicable to similar problems in spite of the high potential of these sources for astrophysical and astrochemical studies. The lack of relevant information might be explained by the peculiar geometry of such systems that are generally characterized by the presence of a pre-expansion chamber where the plasma is initiated before full expansion in the vacuum chamber. This particular configuration tends to complicate the flow parameters calcula-

tions. The goals of this paper are to identify the flow key parameters and help in the design and the use of pulsed planar expansion nozzles widely employed by the atomic and molecular physics community.

The computational flow dynamics model is described in Section 2, followed by a discussion of the results and a comparison with experimental data in Section 3.

## 2. Model

### 2.1. Model description

The critical Reynolds number which corresponds to the transition from a laminar to a turbulent flow is high for bidimensional flows, and not reached under our experimental conditions (moderate backing pressure, small characteristic length, etc.). We therefore consider that the flow is fully laminar. The flow dynamics is modeled by a multiple-block compressible Navier–Stokes solver (MB-CNS), designed for the simulation of transient compressible flows. The program performs the time-integration of the Navier–Stokes equations for two-dimensional compressible flows on a multiple-block structured mesh. The flow geometry may be either planar or axisymmetric and multiply-connected domains can be modeled by patching together several blocks. The flow domain is discretised by a structured grid and a finite-volume approach is used to discretise the conservation equations. A full description of the basic equations and algorithms used for the single-block version of the code may be found in Ref. [20] and the multi-block formulation is documented in Ref. [21].

The flow geometry, the fluid properties (molecular mass, viscosity, thermal conductivity, heat capacity) and the initial conditions (temperature, pressure) are supplied to the program to compute a grid and the physical conditions (Mach number, velocity, temperature, pressure, and mass density) in each point of the grid. Considering the large aspect ratio of the slit (length/width  $\sim 500$ ), we can reasonably neglect the influence of the boundary conditions and scale back the calculations to two dimensions treating the slit as infinitely long. In practice, the uniformity of the expansion is limited by a good distribution of the gas over the whole length of the aperture, mechanical microscopic defects of the slit edges and a good positioning of the electrodes (see Fig. 1). The grid consists of seven blocks composed of a total of 8295 cells.

### 2.2. Flow geometry

The flow geometry is constrained by the shape and the dimensions of the PDN source. The PDN source has been detailed elsewhere [11]. Only the main relevant features are briefly described below. A cross-section of the PDN is shown in Fig. 1. The slit nozzle source, described in Ref. [22], has been designed to produce intense (flow rate of  $8 \text{ cm}^3$  per pulse) and short (1-ms long) gas pulses. The PAH solid sample is disposed in a heated reservoir or oven

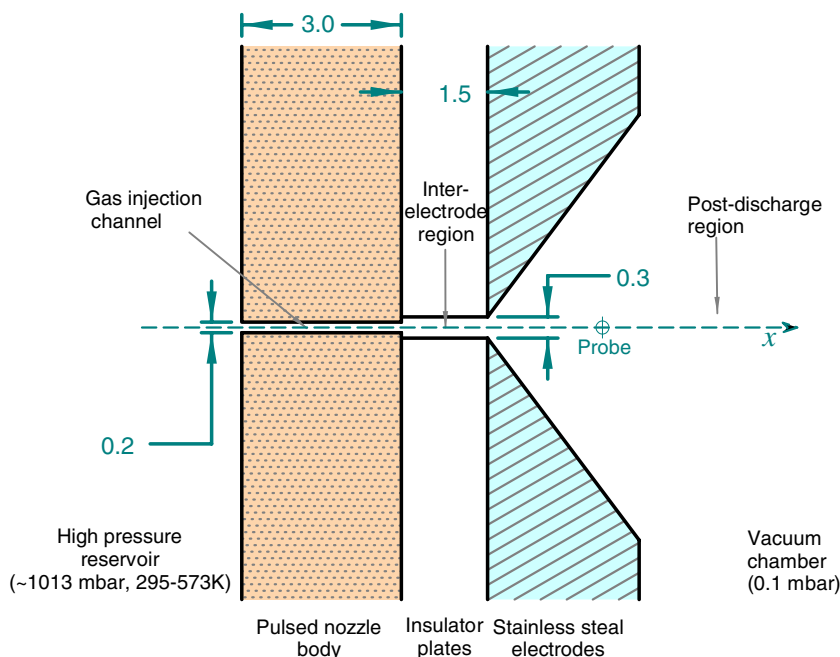


Fig. 1. Close up of the cross-section of the PDN source. The gas expands from a high pressure (and temperature) reservoir (left end side) to a vacuum chamber (right side) through a small single injection channel. A shutter not represented here controls the opening of the channel (gas pulse duration and repetition rate). The units are in mm. Important note: no voltage is applied to the electrodes in the simulation described in this paper. Only the bulk flow is modeled. The laser probe region ( $x = 3.45$  mm) is indicated by a circle.

( $\leq 573$  K) into which a carrier gas is injected and mixes with the PAH vapors. After a short residence time ( $\sim 100$  ms) in the reservoir, the shutter opens (the activation of the three solenoid valves (General Valve Corp.) retracts the poppet that seals the reservoir from the inside) and the thermalized and pressurized ( $\sim 1$  atm.) gaseous mixture ( $< 1\%$  PAH dilution) escapes through a  $100 \text{ mm} \times 0.2 \text{ mm}$  slit into a  $3 \text{ mm}$  long single injection channel. The fluid is then expanded into a larger intermediate cavity ( $100 \text{ mm} \times 0.4 \text{ mm} \times 1.5 \text{ mm}$ ) which harbors the plasma when the discharge is turned on. The walls of the intermediate cavity are made of Macor<sup>®</sup> to insulate the reservoir – which is set to the ground – from the cathode. The cathode is made of two negatively biased stainless steel jaws mounted on each side of the orifice, on top of the insulator plates. The gas finally accelerates and expands into the vacuum chamber, past the cathode, in the so called post-discharge region. A pressure of less than  $2 \times 10^{-1}$  mbar is maintained in the vacuum chamber by a mechanical booster pump with a capacity of 250 l/s. The flow is usually probed at  $x = +3.5$  mm downstream the slit nozzle (2 mm from the cathode).

### 2.3. Fluid properties

The flow dynamics are investigated here for a variety of PAHs diluted either in He or Ar carrier gases. The same approach can be used for any other atomic or molecular species seeded in the expansion. The fluid properties necessary for the computation are gathered in Table 1. The vis-

cosity at a given temperature,  $\mu(T)$ , of all species present in the flow is calculated from the Sutherland viscosity equation [23]:

$$\mu(T) = \mu_0 \left( \frac{T}{T_0} \right)^{3/2} \left( \frac{T_0 + C}{T + C} \right) \quad (1)$$

with  $\mu_0$ , the viscosity at the temperature of  $T_0 = 273$  K and  $C$  the Sutherland constant in Kelvin given in the fourth column of Table 1. The thermal conductivity,  $k$ , is computed assuming a constant Prandtl number,  $Pr$  from the formula:

$$k = \frac{\mu C_p}{Pr}. \quad (2)$$

The thermodynamic properties of a fluid mixture of two gases are computed using effective gas constants and specific heats:

$$\begin{aligned} \bar{R} &= \delta_x R_x + \delta_{\text{PAH}} R_{\text{PAH}}, \\ C_V &= \delta_x C_V^x + \delta_{\text{PAH}} C_V^{\text{PAH}}, \\ C_P &= \delta_x C_P^x + \delta_{\text{PAH}} C_P^{\text{PAH}}, \end{aligned} \quad (3)$$

where  $\delta$  represents the mass fraction of the gas components and the subscript  $x$  denotes the carrier gas type. The coefficients  $R_i$  given in the last column of Table 1 correspond to the ratio  $\bar{R}/M_i$  with  $\bar{R}$ , the universal gas constant and  $M_i$  the molecular weight of the species  $i$ . The viscosity of the fluid mixture is estimated using Wilkes's method with the Hering-Zipperer approximation [24].

$$\mu = \alpha_{\text{PAH}} \mu_{\text{PAH}} + \alpha_x \mu_x \quad (4)$$

with

Table 1  
Fluid properties [28]

Species (formula)	Molar weight (g/mol)	Viscosity, $\mu$		Thermal conductivity, $k$ (mW m <sup>-1</sup> K <sup>-1</sup> )	$Pr$	$C_p$ (J kg <sup>-1</sup> K <sup>-1</sup> )	$C_p/C_v$	$R = \frac{R}{M}$ (m <sup>2</sup> s <sup>-2</sup> K <sup>-1</sup> )
		$\mu_0$ ( $\mu$ Pa s)	$C$ (K)					
He	4.0026	18.64	*	142.64	0.670	5193	1.667	2077.27
Ar	39.948	21.00	144	16.36	0.670	521	1.667	208.13
Naphthalene (C <sub>10</sub> H <sub>8</sub> )	 128.174	5.05	700	54.46	0.748	1035	1.067	64.87
Phenanthrene (C <sub>14</sub> H <sub>10</sub> )	 178.233	4.35	400	39.25	0.651	1047	1.047	46.65
Pyrene (C <sub>16</sub> H <sub>10</sub> )	 202.255	4.35	300	33.70	0.635	995	1.043	41.11

\* For He, the viscosity is calculated from the  $\mu = \mu_0 \left(\frac{T}{T_0}\right)^{0.647}$  equation [20,23,24].

$$\alpha_{\text{PAH}} = \left[ 1 + \frac{\delta_x}{\delta_{\text{PAH}}} \sqrt{\left(\frac{M_{\text{PAH}}}{M_x}\right)} \right]^{-1} \quad (5)$$

and

$$\alpha_{\text{PAH}} + \alpha_x = 1, \quad (6)$$

where  $M_{\text{PAH}}$  and  $M_x$  are the molecular weights of PAH and Ar or He carrier gases, respectively. The thermal conductivity of the gas mixture is calculated using the same weighting scheme.

### 3. Results and discussion

In Section 3.1, we present and discuss the flow modeling results obtained in the stationary regime for different gas mixtures and initial reservoir temperatures. It is followed by the calculations of the flow dynamics for pure carrier gases and PAH containing gas mixtures. Sections 3.2 and 3.3 are respectively devoted to the boundary layers and the dynamics of the supersonic expansion. Finally, in Section 3.4, we examine the change of flow characteristics when the geometry – inter-electrode length – is altered to help optimize future experiments.

#### 3.1. Flow simulation in the stationary regime

The results reported in this section have been obtained for long hydrodynamic times ( $>1$  ms), close to the stationary regime. The calculation domain is restricted to the upstream part of the zone of silence (about 20 times the slit width) of the supersonic expansion [25] away from the Mach disk. According to Beylich [26], the Mach disk position of a supersonic planar expansion,  $x_M$  can be estimated by the relation:

$$\frac{x_M}{d} = \frac{3}{2} \sqrt{\frac{P_0}{P_b}} \left(\frac{L}{d}\right)^\varepsilon \quad (7)$$

with  $d$ , the slit width,  $L$  the slit length,  $P_0$ , the stagnation pressure,  $P_b$ , the background pressure, and  $\varepsilon$ , an empirical coefficient that can vary between 0.47 and 0.735, the lower values corresponding to large length to width ratios. The visual examination of the extent of the luminous plasma expansion reveals no discontinuity along the  $x$  axis in the

flow. It suggests that the front of the shockwave is materializing close to the wall. This is expected because under our experimental conditions where  $P_0/P_b \sim 6000$ , the calculated Mach disk position exceeds the dimensions of the chamber ( $>0.6$  m).

##### 3.1.1. Flow characteristics for pure gases

The examination of the two-dimensional contour maps of a typical Ar flow displayed in Fig. 2 immediately leads to the identification of three zones that are superposed to physical regions: (1) the gas injection channel – opened up by the mechanical shutter, (2) the inter-electrode region and (3) the post-discharge region. The gas flows adiabatically in the injection channel, which possesses a steady, constant area. As the gas expands in the channel, it uses its pressure to overcome the energy dissipated by the viscous friction on the walls during its journey. Fanno flow is the term given to adiabatic gas flow with friction in a pipe of constant section [27]. The conductance loss caused by wall friction triggers a sequence of events starting with: (i) a pressure drop along the pipe that causes (ii) a fall of the number density. The reduction in density causes (iii) the velocity to rise. The rise in velocity raises (iv) the kinetic energy of the gas. To maintain the energy balance, the rise in kinetic energy is compensated for by (v) a reduction of the enthalpy. The reduction in enthalpy causes a drop in temperature. All these effects can also be visualized in Fig. 3. The rise in entropy associated to this evolution achieves its maximal value at the exit of the injection channel where the gas velocity reaches the value of the local acoustic speed.

At the exit of the injection channel (zone 1), the flow enters in a pipe with a larger but still constant cross-section: the inter-electrode region (zone 2). This sudden section change provokes the expansion of the gas which becomes supersonic with Mach values that reach 2.5 in the first 200  $\mu\text{m}$ . The wall friction has for effect this time to compress the fluid. The conductance loss causes a velocity drop that is followed by a rise in density and pressure (Fanno flow with supersonic initial conditions). The length of this channel is too small to generate a large conductance loss which would prompt a change of regime (subsonic).

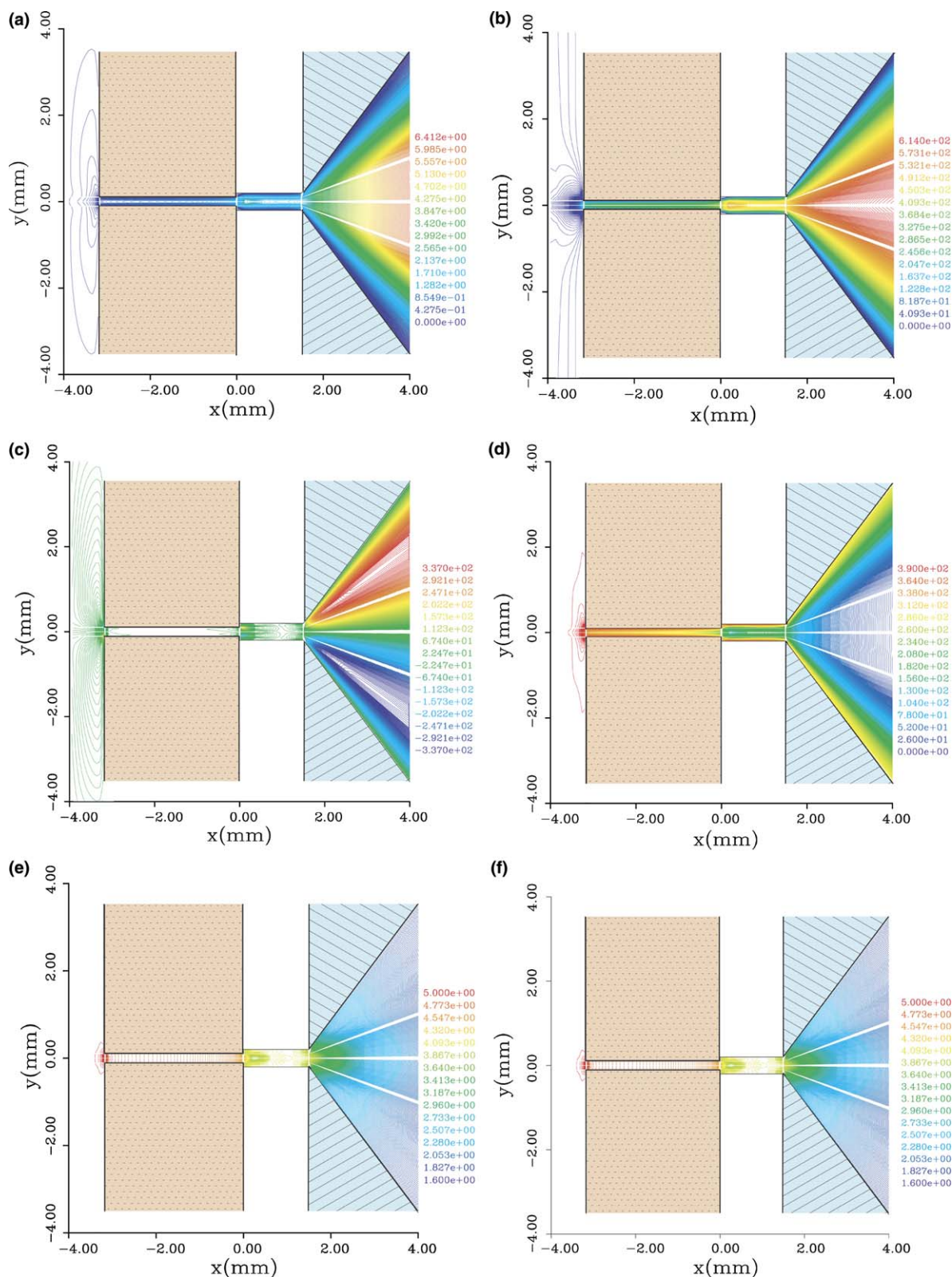


Fig. 2. Contour maps of the thermodynamic parameters. (a) Mach number: the flow becomes supersonic ( $M = 1$ ) at the exit of the gas injection channel and is accelerated to achieve  $M \sim 6$  at about  $x = 4$  mm. The dark blue region outlines the subsonic region, (b) axial speed: the flow is very close to its terminal velocity at about  $x = 4$  mm downstream ( $>600$  m/s). The axial velocity shows a strong radial gradient, (c) radial speed: this component of the velocity is without surprise minimum along the axis. (d) Temperature: it drops from 390 K in the reservoir to 26 K at  $x = 4$  mm downstream. Note that the flow's temperature is quite homogenous in the zone of silence. (e) The flow density ( $\text{kg/m}^3$ , log scale) map reveals three zones and varies over two orders of magnitude. (f) The pressure (Pa, log scale) drops over more than three orders of magnitude. Here again, we identify very distinctly three zones. These maps are obtained for a pure Ar flow with a reservoir pressure of 1 atm and a temperature of 390 K and calculated for long hydrodynamic times. (For interpretation of the references to colour in this figure legend, the reader is referred to the web version of this article.)

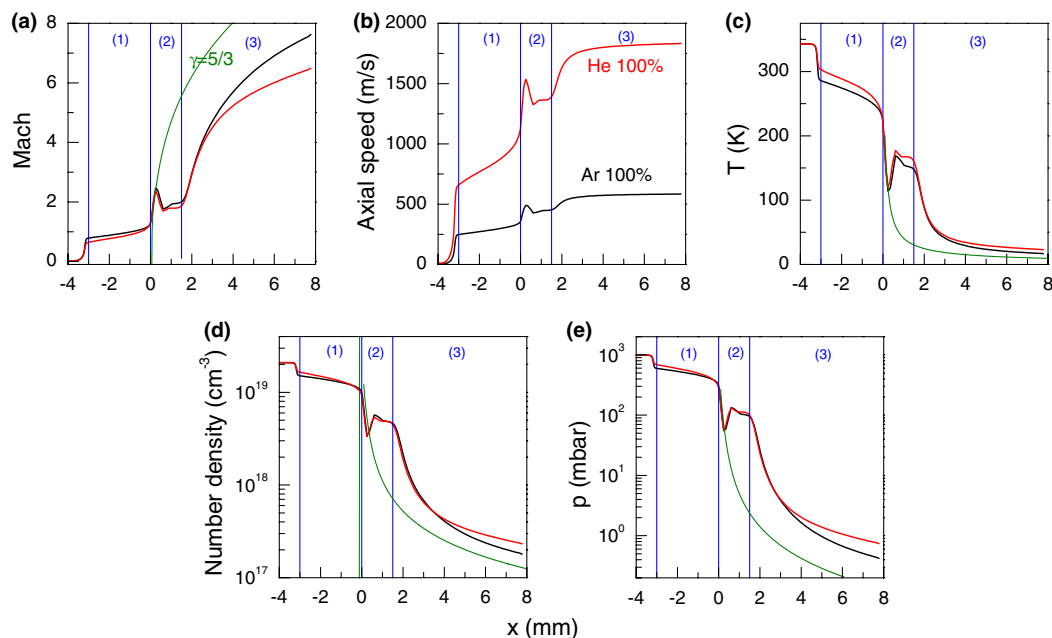


Fig. 3. (a–e) Profiles of the thermodynamic parameters along the axis centreline obtained for pure carrier gases with reservoir pressure of 1 atm. and a temperature of 343 K and calculated for long hydrodynamic times. We can distinguish three zones superposed to the physical regions: (1) the gas injection channel – opened up by the shutter, (2) the inter-electrode region and (3) the post-discharge region. The dotted lines correspond to calculated profiles of a 2D expansion produced by a slit aperture infinitely thin under the same conditions and for a monoatomic carrier gas ( $\gamma = 5/3$ ) from equations detailed in Ref. [24]. The calculated profiles of the thermodynamic parameters of the PDN are not only shifted on the  $x$  axis from the isentropic flow behavior (dotted line) but also follow a different trend and diverge from each other far downstream.

A more quantitative picture is provided by the profiles along the flow axis centreline calculated for pure carrier gases of Ar and He and shown in Fig. 3. As explained above, the flow area is constant in the gas injection channel and the major driving potential affecting the thermodynamic states of the fluid is the wall friction. The temperature, pressure and number density all decay adiabatically in this channel. Because of the large stagnation pressure in the reservoir, the flow is choked at the slit exit plane (Mach = 1). The sudden growth of the Mach number in the first  $\sim 200 \mu\text{m}$  is followed by a drop off in the next  $\sim 200 \mu\text{m}$  (Fig. 3a). This behavior is caused by the shockwave produced by the compression of the expansion by the walls of the inter-electrode region (separated by only 0.4 mm). The Mach number gradually rises in the remaining 1.1 mm to achieve Mach 2 at the tip of the cathode. The gas then expands into the post-discharge zone, characterized by the typical behavior (in a first approximation) of planar expansions. The axial speed profile (Fig. 3b) shows that the atoms or molecules that compose the gas travel substantially more rapidly through the IE region in He (1.1  $\mu\text{s}$ ) than in Ar (3.6  $\mu\text{s}$ ) mixtures by a factor over 3. In other words the residence time in the plasma is seriously shortened in He and offers less time for chemistry to take place. The axial speed increases downstream the cathode to reach the terminal velocity (598 and 1887 m/s for Ar and He respectively for a reservoir temperature of 343 K) when all the internal enthalpy has been transformed in kinetic energy. The number density and pressure profiles

of Ar and He (Fig. 3d,e) flows remain very similar in the  $[-4 \text{ mm}, +3.5 \text{ mm}]$  range. Beyond the upper value of 3.5 mm, both curves start to diverge. Regarding the temperature (Fig. 3c), we observe differences in the inter-electrode region where the He flow is warmer by  $\sim 10 \text{ K}$ . The temperature profiles also point to a slightly warmer temperature for He in the post-discharge region.

### 3.1.2. Flow characteristics for gas mixtures

The logical following step consists of determining the impact on the characteristics of the He and Ar flows of the injection of a small amount of PAHs. Calculations have been performed for a selection of PAHs – Naphthalene ( $\text{C}_{10}\text{H}_8$ ), Phenanthrene ( $\text{C}_{14}\text{H}_{10}$ ) and Pyrene ( $\text{C}_{16}\text{H}_{10}$ ) – diluted in Ar or He carrier gases for different initial conditions. In the current simulation as well as for most experimental setups, the dilution, which corresponds to the ratio of the PAH vapor pressure with the total gas

Table 2  
Reservoir temperatures that are required to achieve 1% and 5% PAH dilution at  $p = 1 \text{ atm}$ .

Species	Reservoir temperature (K)	
	1% Dilution	5% Dilution
Naphthalene	343	390
Phenanthrene	437	487
Pyrene	494	535

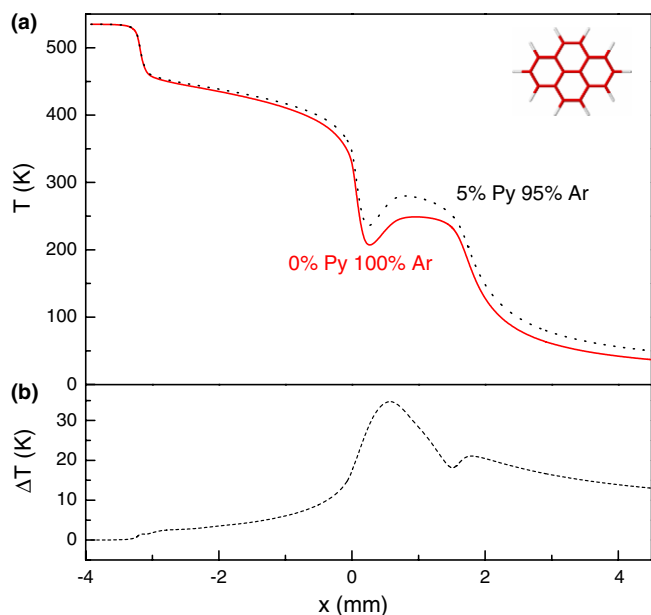


Fig. 4. The injection of a significant amount of Pyrene ( $C_{16}H_{10}$ ) in an Argon flow (5%) causes a significant heating in the inter-electrode (35 K,  $\Delta T/T \sim 13\%$ ) and post-discharge (15 K,  $\Delta T/T \sim 25\%$ ) regions. This heating effect is less pronounced in He flows. (a) Temperature profiles of Py/Ar gas mixtures calculated for a backing pressure of 1 atm. and a reservoir temperature of 535 K. (b) Residual.

pressure, is dependent on the reservoir temperature. The PAH vapor pressure is calculated from the Antoine equation with the coefficients taken from Ref. [28]. Calculations have been made for PAH dilution of 1% and 5% – the latest being an extreme case – which are associated with two different temperatures for each PAH compound as indicated in Table 2.

The temperature appears to be a sensitive tracer as illustrated by the profiles calculated in the presence and absence of Pyrene in Argon and shown in Fig. 4.

The most quantitatively affected region is the inter-electrode region (IER) where the heating can reach 35 K or almost 13% in presence of 5% of Pyrene diluted in Ar. The heating affects also the post-discharge region (PDR) where the temperature sees its value increase by more than 13 K or  $\Delta T/T \sim 25\%$ .

The temperature, number density and axial speed characteristics calculated for different PAH/Argon and PAH/Helium mixtures for two different positions along the flow are gathered in Fig. 5. The first position at  $x = +0.88$  mm downstream the nozzle is at the heart of the IER. The second one at  $x = +3.45$  mm from the slit nozzle in the post discharge region corresponds to the spectroscopic probe area. The detailed inspection of the results reveals that the injection of PAH causes heating in the IE and PD regions in both Helium and Argon flows. This effect is much more pronounced for the post-discharge region of Argon flows in which the cooling becomes inefficient for high PAH concentration. Even at the low concentration

of 1%, the heating can reach almost 5 K for Pyrene (2%) in the inter-electrode zone and 3 K in the PDR ( $>5\%$ ).

Also, the flow undergoes a total number density drop upon injection of PAH. This time, the effect is more marked for Helium flows. Consequently, the PAH number density in the probe region only doubles when the PAH concentration in the reservoir goes from 1% to 5%. From an experimental standpoint, it means that the detection signal in the supersonic expansion exhibits a non linear response with PAH concentration in the reservoir. Thus increasing the PAH concentration will only lead to a moderate increase in the detected signal. The real gas behaviour will likely be worse than that predicted because of exothermic condensation to clusters of various sizes in the jet [19] especially for high PAH concentrations.

Besides, we observe that the flow is slowed down in the IER for both carrier gases. The velocity drop goes from 6 m/s for Naphthalene/He (1%) to 36 m/s for Naphthalene/He (5%) and from 1 m/s for Naphthalene/Ar (1%) and 5 m/s for Naphthalene/Ar (5%). Interestingly, the flow is significantly slowed down in the post-discharge in Helium whereas it is moderately accelerated in Argon. This different behavior is explained by the modification upon PAH injection of the internal enthalpy of the carrier gas, and eventually the limit velocity  $v_\infty = (2C_p T)^{0.5}$ . The inequality between the specific heats of all species involved,  $C_p(\text{He}) > C_p(\text{PAH}) > C_p(\text{Ar})$ , produces an increase of the limit velocity in Argon and a small drop in Helium.

The temperature, number density and velocity variations depend strongly on the dilution (i.e. the reservoir temperature) but much less on the nature of the PAHs. The flow characteristics, not detailed here, calculated for different PAHs for the same dilution and reservoir conditions (decoupling of dilution and reservoir temperature) are very close as they essentially depend on the ratio of the specific heats,  $\gamma$ , which is almost identical for the selected PAHs.

The probe temperature of 46 K calculated for a pure Argon flow with a reservoir temperature of about 487 K is consistent with the findings of a recent experiment using the same pulsed slit nozzle source for the preparation of jet-cooled Perylene ( $C_{20}H_{12}$ ) and a cavity ring down spectrometer for the detection. In that study, a temperature of 52 K is derived from the analysis of the rotational contour of the vibronic band associated with the  $S_1 \leftarrow S_0$  (0–0) transition of Perylene which was highly diluted in Argon (0.015%) at a reservoir temperature of 480 K [29]. This comparison with the experimental data reveals that the relaxation of PAH molecules by collisions with Ar atoms is fully efficient.

In summary, the simulations indicate that the injection of large amounts (5%) of PAHs raises significantly the temperature of Ar flows and drops the total number density in the post-discharge regions of He flows. These effects are probably underestimated because clustering is not taken into account in our simulations.

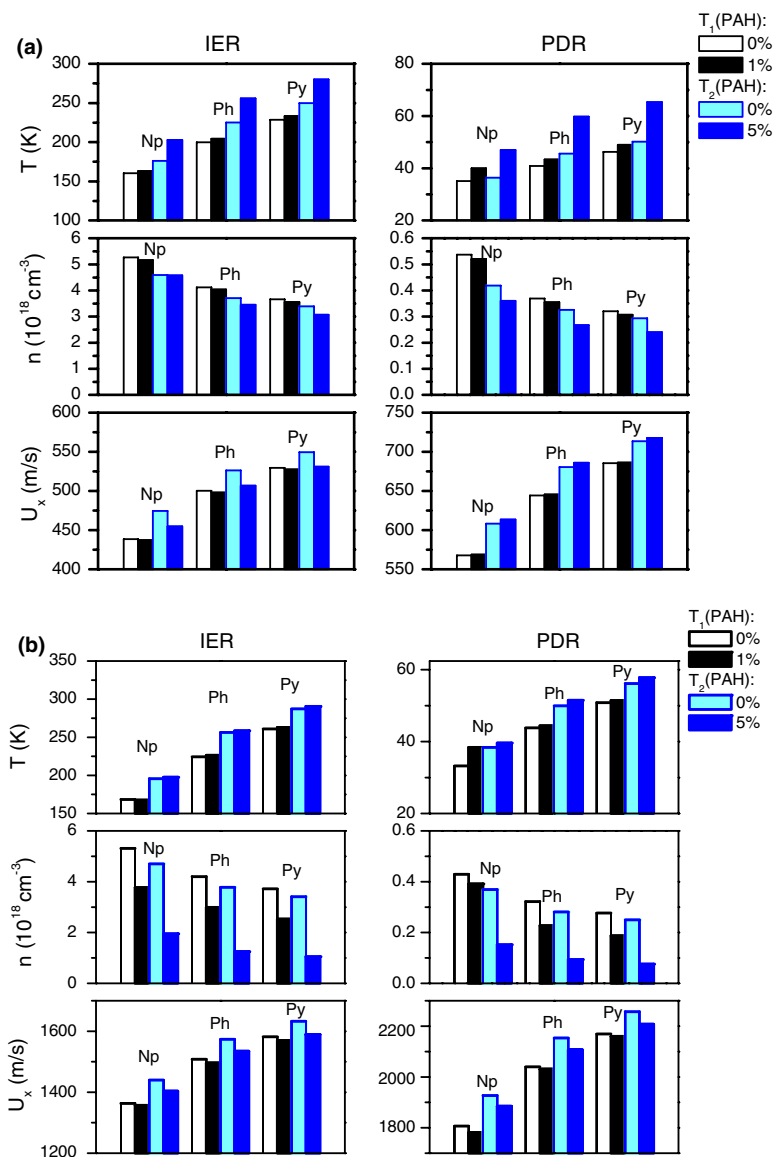


Fig. 5. Flow characteristics for: (a) PAH/Ar and (b) PAH/He gas mixtures. In the current simulation as well as for most experimental setups, the reservoir temperature governs the PAH dilution. Calculations have been made for PAH dilution of 1% and 5% which represent two different temperatures for each PAH compound as indicated in Table 2. The PAH injection generates: (i) the heating of the IE and PD regions, (ii) a drop of the total number density, quite dramatically in the PD region for He flows and (iii) the global slow down of the He flow, a slow down of the Ar flow in the IE, and an acceleration in the PD region.

### 3.1.3. Flow characteristics vs. reservoir temperature, pressure and density

The reservoir temperature, that governs the PAH dilution ratio in the carrier gas, can be varied over a wide range to achieve an adequate vapor pressure for the PAH under study. The modification of the initial thermodynamic conditions (temperature  $T_0$ , pressure  $p_0$  and density  $\rho_0$ ) affect appreciably the physical parameters downstream the nozzle.

As illustrated in Fig. 5 for pure carrier gases (i.e. white and light blue columns), the temperature and number density exhibit the steepest dependence on the reservoir temperature. In particular the number density is almost cut

by two when the reservoir temperature goes from 343 to 560 K. This has to be kept in mind when one searches for the signal, generally proportional to the number density, during the optimization phase of an experiment. We also observe that the dependence is more marked for axial speed and temperature in He. The raise of the axial speed is however insufficient to affect substantially the short residence time in the IER.

In an isentropic (i.e. no heat transfer with the surroundings) flow of a perfect gas, the pressure, temperature and density in the expansion can be described by the initial conditions ( $T_0$ ,  $P_0$ ,  $\rho_0$ ), the ratio of specific heats, and the local Mach number from the equations:

$$\begin{aligned}\frac{T_0}{T} &= \left(1 + \frac{\gamma - 1}{\gamma} M^2\right), \\ \frac{P_0}{P} &= \left(1 + \frac{\gamma - 1}{\gamma} M^2\right)^{\frac{\gamma}{\gamma - 1}}, \\ \frac{\rho_0}{\rho} &= \left(1 + \frac{\gamma - 1}{\gamma} M^2\right)^{\frac{1}{\gamma - 1}}.\end{aligned}\quad (8)$$

The density  $\rho$  is related to the number density by the equation:

$$\frac{n}{N_{\text{Avo}}} = \frac{\rho}{M_x(1-f) + M_{\text{PAH}}(f)} \quad (9)$$

with  $f$  the fraction of the PAH diluted in the carrier gas  $x$ , and  $N_{\text{Avo}}$ , the Avogadro number. In our experiment, the flow in the areas (1) and (2) is not isentropic and the downstream thermodynamic parameters cannot therefore be directly predicted. In this paragraph, we attempt to predict the local conditions in the planar expansion in function of the reservoir conditions.

Flow calculations have been carried out for seven reservoir temperatures (343, 428, 437, 487, 494, 535 and 560 K) at the pressure of 1 atm. and for three different pressures (0.5, 1 and 1.5 atm.) at the temperature of 343K for pure argon and helium gases. The results are gathered in Fig. 6, which displays the flow centreline local Mach number versus the  $T_0/T$ ,  $P_0/P$  and  $\rho_0/\rho$  ratios. The isentropic expansion behaviour is also represented for comparison. We observe an excellent agreement between all the simulation data curves (different reservoir conditions) and the isentropic curve for the temperature ratio. This is predict-

able because Fanno and isentropic flows exhibit the same Mach number dependence for  $T_0/T$ .

However, the pressure and density ratios evolution diverge sensibly from the isentropic expansion case. The density ratio starts to diverge from Mach 2 which corresponds to the beginning of the post-discharge zone. The gap from the isentropic curve increases with the Mach and is more marked for Helium flows despite an identical specific heat ratio ( $\gamma = 1.667$ ). Finally, the figure reveals a significant spread between the simulation data curves that is more pronounced again for Helium flows with a divergence that increases with the reservoir temperature. The evolution of the pressure ratio follows a pattern similar to the density ratio, although not as strongly divergent. We conclude that we can reasonably use the isentropic equation to predict the local temperature from initial conditions but not the local density and pressure. In those cases, one has to refer to the curves displayed in Fig. 6 to estimate how the local variables depart from an isentropic behaviour.

### 3.2. Boundary layers

The velocity grows from zero at the wall surface to a maximum at a certain height. The height needed to achieve 99% of the mainstream velocity is defined as  $\delta$ . It represents the boundary layer thickness. As a consequence, we can define  $\lambda(x) = [L(x) - 2x\delta(x)]$ , the extent of the domain where the velocity is above 99% of its mainstream value (see insert of Fig. 7), with  $L(x)$  the distance between the walls.

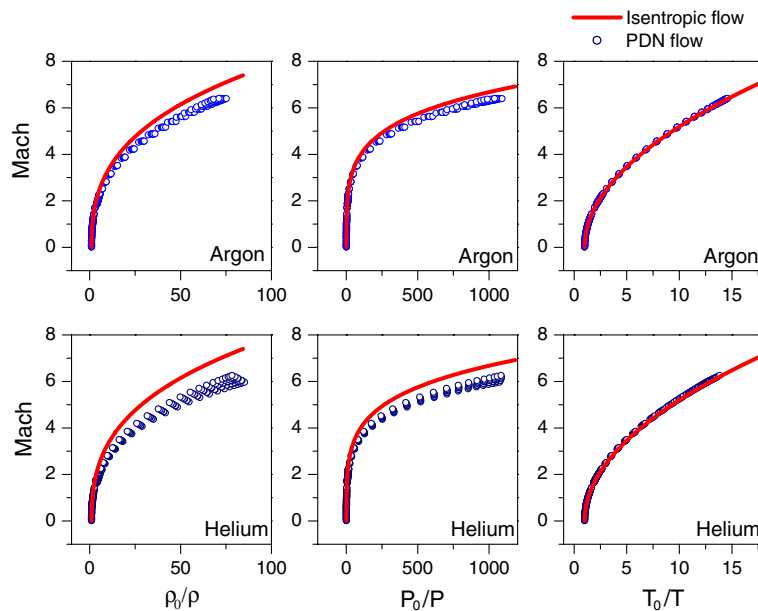


Fig. 6. Flow centreline local Mach number versus the  $T_0/T$ ,  $P_0/P$  and  $\rho_0/\rho$  ratios. Calculations have been carried out for seven reservoir temperatures (343, 428, 437, 487, 494, 535 and 560 K) at the pressure of 1 atm. and for three different pressures (0.5, 1 and 1.5 atm.) at the temperature of 343 K for pure argon and helium gases. The isentropic expansion behaviour is also represented (red line) for comparison. We note that if the Mach number profile  $M(x)$  is known, one can reasonably well predict the stream temperature. However, the density centreline profile is much less predictable from the isentropic flow behaviour especially far downstream ( $M(x) > 3$ ). (For interpretation of the references to colour in this figure legend, the reader is referred to the web version of this article.)

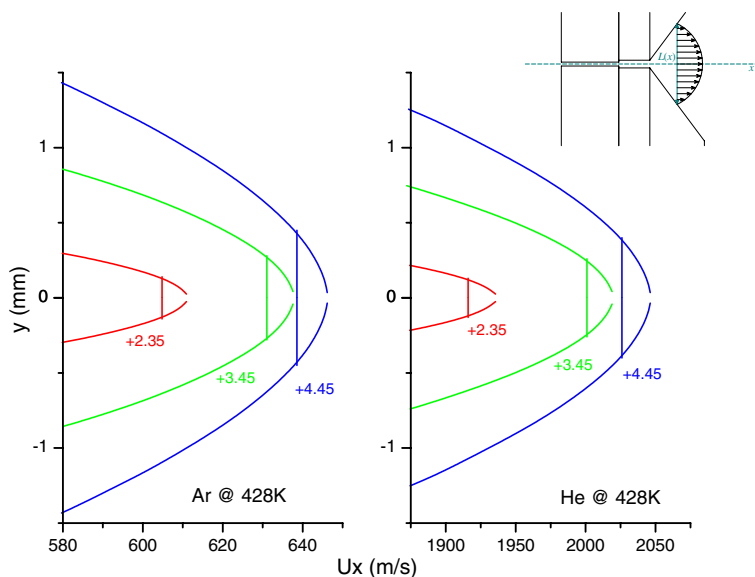


Fig. 7. Homogeneous flow conditions and boundary layers. The axial speed is calculated for different positions  $x$  in the flow for pure He and Ar gases at a reservoir temperature of 428 K. The extent of the domain where the velocity is above 99% of its mainstream value,  $\lambda$ , grows with the distance from the nozzle to achieve 1/2 mm at  $x = +3.45$  mm. It outlines a homogeneous region suited for instance for laser probing. Inset: cross-section of the source. The length  $L(x)$  represents the distance between the walls. The arrow length represents the amplitude of the axial speed which converges to zero close to the walls.

Fig. 7 shows the axial speed calculated for different positions  $x$  in the flow for pure He and Ar gases at a reservoir temperature of 428 K. The mainstream thickness  $\lambda(x)$ ,

grows from 0.28 mm at the position  $x = +2.35$  mm to 0.90 mm at  $x = +4.45$  mm. At the probe position of  $x = +3.45$  mm, the axial speed has reached 94.5% and

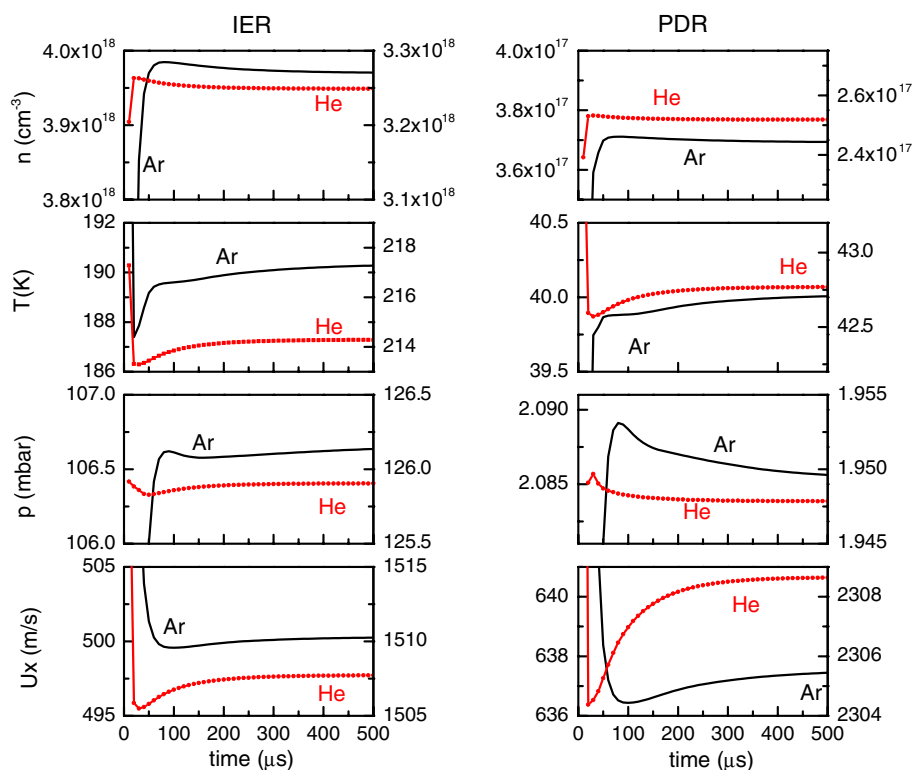


Fig. 8. Dynamics of the number density, temperature, pressure and axial speed in pure Ar (left  $y$ ) and He (right  $y$ ) flows in the IE and PD regions. Calculations are done for initial temperature of 428 K and pressure of 1 atm. The flow is established and stable within 75 and 25  $\mu\text{s}$  for Ar and He, respectively. These values are well below typical laser delay (see Ref. [11]) ensuring that the flow is uniform during the time window it is probed.

94.9% of the terminal velocity,  $\sqrt{2C_p T}$ , in Ar and He respectively and the mainstream thickness is in the 0.5–0.6 mm range. It means that the laser, which has a beam diameter of  $\sim 1.5$  mm, will probe a larger and more inhomogeneous area characterized by a velocity above  $\sim 90\%$  of its mainstream value. This result may justify the experimental need for an accurate alignment procedure.

### 3.3. Flow dynamics

The investigation of the flow *dynamics* is important to establish the time it takes for the flow to reach the equilibrium. One of the aims is to help define a time window under which one can probe molecules in a stable environment. The evolution of the thermodynamic parameters of a set of cells of the grid is recorded over time to investigate the flow dynamics. The cells are chosen at the heart of the inter-electrode region,  $x = +0.88$  mm, and in the post discharge region,  $x = +3.45$  mm. Typical curves of the density, temperature, pressure, and axial speed, displayed in Fig. 8, indicate that it takes about 75 and 25  $\mu\text{s}$  in Ar and He respectively for the flow conditions stabilize within 1% of their equilibrium values. It requires then at most 400 and 180  $\mu\text{s}$  in Ar and He, respectively, for the flow parameters to reach 99.9% of their equilibrium values.

For comparison with experimental measurements, it is necessary to make the assumptions that the number of electrons extracted by the electrical potential – when the discharge is set on – is roughly proportional to the carrier gas number density and that the discharge can be established much faster than the flow (electrons travel much more rapidly than neutral Ar or He atoms). One can then acquire a “picture” of the gas pulse by monitoring the discharge current while scanning the gas pulse duration (by varying the delay between the shutter opening and the firing of the discharge). The experimental observations suggest stabilization times of the same order of magnitude (i.e. about 100  $\mu\text{s}$ ) in Argon flow under similar initial conditions. The discrepancy between calculations and observations is not surprising as the reservoir pressure may for instance experience sudden fast variations upon the opening of the shutter in absence of a mass flow controller.

### 3.4. Inter-electrode region length

In this section, we calculate the flow characteristics for different inter-electrode region lengths and discuss the possible implications for the plasma. When the plasma is turned on, neutral precursor molecules (PAH) are bombarded during their flight in the inter-electrode region by electrons, ionized and metastable atoms from the carrier gas – which may lead to ionization by electron impact, charge transfer or Penning ionization, respectively. Prior studies have led to the identification of three factors that affect the PAH ion yield. The first one is the plasma

energy determined mainly by the discharge voltage. We have shown that the PAH ion signal reaches a maximum for an applied voltage of  $-500$  V and decreases thereafter [11]. We have experimental evidence that excessively high discharge currents promote PAH fragmentation and formation of PAH clusters through ion-neutral reactions at the expense of the PAH ion yield. The second factor is the nature of the carrier gas. Our measurements hint at a key role for Penning ionization. Under this scenario, the ion yield would depend in part on the energy difference between the PAH ionization potential and the populated energy level of the metastable atom. The role of Penning ionization is confirmed by numerical simulations of the plasma that are described in separate papers [17,18]. The results show that metastable Ar atoms are more abundant in the plasma by more than one order of magnitude than electrons with an energy above the PAH ionization potential. Therefore, the production of PAH cations by Penning ionization should dominate over electron impact ionization assuming cross-sections of the same magnitude based on the scarce data available (i.e.  $4.23 \times 10^{-20} \text{ m}^2$  for Penning ionization of  $\text{C}_{60}$  with  $\text{Ar}^*$  ( $4p^3D_3$ ) and  $<10^{-20} \text{ m}^2$  for electron impact ionization (12 eV) of  $\text{C}_{60}$  [30,31]). Finally, it is reasonable to assume that the yield of PAH ions is tightly linked to the residence time in the reactor. We have shown in Section 3.1.1 that the residence time in the reactor is seriously shorter in He than in Ar flows. This effect may also contribute to reduce the PAH ion yield in Helium flows as compared to Argon flows.

Based on all these considerations we expect that increasing the plasma length will raise not only the precursor residence time but also the breakdown voltage necessary to initiate the plasma and the voltage to maintain a stable discharge. So the evolution of the PAH ion yield will depend of a subtle balance between the plasma length (residence time) and the plasma energy (discharge current).

Flow calculations have been carried out for different inter-electrode lengths in pure Ar while keeping all other parameters fixed. The Mach number, number density and temperature versus the inter-electrode length are displayed in Fig. 9. The flow remains supersonic in the inter-electrode region for lengths under 27 mm. The first observation is that the average inter-electrode region temperature depends nearly linearly on the length of the region. We also remark that the number density is increased by about 30% when the length goes from 1.5 to 27 mm. Finally, we find out that the Mach number is divided by two when the length is multiplied by 18. It implies that the residence time of the molecules in the active region, where most of the ionization and chemistry take place, is multiplied by almost 40. However, it is expected that the breakdown voltage would become quickly too high with increasing length. Based on these results, we will, in the next step, turn to plasma modeling to find out how the plasma energy is affected by the change in length.

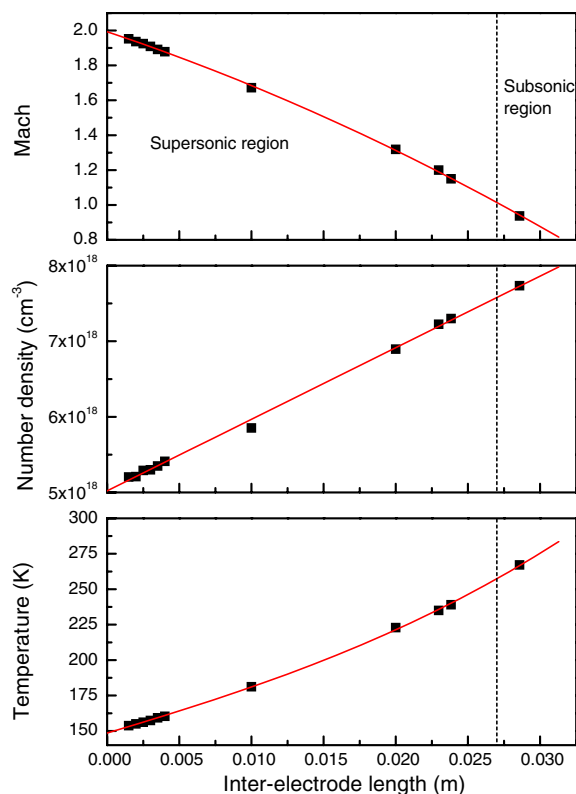


Fig. 9. Average temperature, number density and Mach number versus the inter-electrode region length. The flow remains supersonic under lengths of 27 mm. Calculations have been carried out for Ar flow only. Initial conditions are  $p_0 = 1$  atm. and  $T_0 = 343$  K. See Section 3 for details.

#### 4. Conclusion

The flow produced by a pulsed discharge slit nozzle has been investigated dynamically for a variety of gas mixtures and initial conditions. This work has generated identifiable output, such as the gas number density, pressure and temperature in the inter-electrode region, which have been recently successfully used to feed a state of the art plasma modeling program [17,18]. Because of the weak ionization state of the plasma, we can safely assume that the plasma has no significant influence on the flow characteristics and model the flow independently. Our intention is to provide useful information for designing pulsed discharge slit nozzles which are bound to develop because of their potential for generating species of astrochemical and astrophysical interests. This methodology can be easily generalized to model the flow dynamics behavior of expansions that are seeded with any other atomic or molecular species.

The conclusions drawn from this study for jet expansions seeded with heavy molecules are the following:

- First of all, the residence time in the IE region (or antechamber for other systems) is considerably shorter in He (1.1  $\mu$ s) than in Ar (3.6  $\mu$ s). It implies that the heavy molecular species diluted in the He carrier gas have less

time to undergo chemical/physical changes after the discharge is fired regardless of the mechanisms of molecular ion production.

- The He flow temperature is mildly affected by the injection of traces of heavy molecular species. At the opposite, the injection of large amounts of heavy molecules heats dramatically Ar flows.
- The PAH detection signal downstream exhibits a non linear relation with the PAH concentration in the reservoir (governed by the temperature). This effect is more pronounced for He flows. Also, high molecular concentration (high reservoir temperature) is likely to favor the formation of clusters in the jet which will cause the number of free seeded molecules to drop (producing a proportional drop in the signal).
- Comparisons with experimental data show that the PAH collisional relaxation with Argon atoms is fully efficient.
- The total number density is negatively affected by an increase in the sample reservoir temperature.
- The local temperature can be predicted from the initial conditions using the isentropic equation if the local Mach number is determined. It is highly unreliable however to predict the local pressure and density because they diverge significantly from an isentropic flow behavior. If the centerline Mach number,  $M_{PDN}(x)$  is unknown, it can be approximated by  $M(x + l_{IE})$  calculated for an isentropic flow with  $l_{IE}$ , the inter-electrode length. This method which can be used to predict the local temperature fails farther downstream.
- The calculated extension of the boundary layers suggests that the laser beam will probe a quasi-uniform and stable region in Ar and He expansions.
- The analysis of the dynamics indicates that the flow is established and stable within 75 and 25  $\mu$ s for Ar and He, respectively. These values are well below the laser delay ensuring that the flow is uniform during the time window it is probed.
- Finally, the investigation of the flow for different geometries reveals that the flow characteristics vary slowly with the inter-electrode length. The residence time can thus be enhanced by augmenting the inter-electrode length even by a small amount and without modifying considerably the *bulk* flow properties. However, plasma modeling is required to establish the dependence of the electron energy on the IE length. We indeed expect that the IE length cannot be excessively enhanced because the breakdown voltage necessary to initiate the plasma depends quasi linearly on this length. High breakdown voltages imply high discharge currents to sustain the plasma which may favor fragmentation over soft Penning ionization.

Preliminary studies have shown that the PAHs form clusters in the jet [11]. Further work will try to build a new approach to include the PAH condensation in the calculations of the flow characteristics.

## Acknowledgements

L.B. acknowledges the support from the National Research Council and the SETI Institute from which he benefited at the early phase of the project. A.B. thanks Dr. Peter Jacobs (University of Queensland, Australia) for his very useful numerical program MB\_CNS. This work was supported by NASA Science Mission Directorate/APRA Program.

## References

- [1] Th. Henning, F. Salama, *Science* 282 (1998) 2204.
- [2] J.L. Puget, A. Léger, *Ann. Rev. Astron. Astrophys.* 27 (1989) 161.
- [3] L.J. Allamandola, A.G.G.M. Tielens, J.R. Barker, *Astrophys. J. Suppl. Ser.* 71 (1989) 733.
- [4] T.P. Snow, *Spectrochim. Acta, Part A* 57 (2001) 615.
- [5] F. Salama, in: L. d'Hendecourt, C. Joblin, A. Jones (Eds.), *Solid Interstellar Matter: The ISO Revolution*, EDP Sciences, Springer, Les Ulis, 1999, p. 65.
- [6] J.P. Maier, in: S. Pfalzner, C. Kramer, C. Staubmeier, A. Heithausen (Eds.), *The Dense Interstellar Medium in Galaxies*, Springer Proceedings in Physics, vol. 91, Springer, Berlin, 2004, p. 55.
- [7] E. Witkiewicz, H. Linnartz, C.A. de Lange, W. Ubachs, A. Sfounis, M. Massaouti, M. Velegrakis, *Int. J. Mass Spectrom.* 232 (2004) 25.
- [8] S. Davis, D.T. Anderson, G. Duxbury, D.J. Nesbitt, *J. Chem. Phys.* 107 (1997) 5661.
- [9] T. Motylewski, H. Linnartz, *Rev. Sci. Instr.* 70 (1999) 1305.
- [10] D. Romanini, L. Biennier, F. Salama, A. Kachanov, L.J. Allamandola, F. Stoeckel, *Chem. Phys. Lett.* 303 (1999) 165.
- [11] L. Biennier, F. Salama, L.J. Allamandola, J.J. Scherer, *J. Chem. Phys.* 118 (2003) 7863.
- [12] L. Biennier, F. Salama, M. Gupta, A. O'Keefe, *Chem. Phys. Lett.* 387 (2004) 28.
- [13] O. Sukhorukov, A. Staicu, E. Diegel, G. Rouillé, Th. Henning, F. Huisken, *Chem. Phys. Lett.* 11 (2004) 259.
- [14] T. Pino, N. Boudin, P. Bréchnignac, *J. Chem. Phys.* 111 (1999) 7337.
- [15] J. Oomens, A.G.G.M. Tielens, B.G. Sartakov, G. von Helden, G. Meijer, *Astrophys. J.* 591 (2003) 968.
- [16] J. Rémy, L. Biennier, F. Salama, *Plasma Sources Sci. Technol.* 12 (2003) 295.
- [17] B. Broks, W. Brok, J. Remy, J. van der Mullen, A. Benidar, L. Biennier, F. Salama, *Phys. Rev. E* 71 (2005) 036409.
- [18] B. Broks, W. Brok, J. Remy, J.A.M. van der Mullen, A. Benidar, L. Biennier, F. Salama, *Spectrochim. Acta Part B* 60 (2005) 1442.
- [19] M. Sulkes, C. Jouvet, S.A. Rice, *Chem. Phys. Lett.* 87 (1982) 515.
- [20] P.A. Jacobs, ICASE Interim Report 18, NASA Langley Research Center, 1991.
- [21] P.A. Jacobs, Department of Mechanical Engineering, Research Report 10/96, The University of Queensland, 1996.
- [22] K. Liu, R.S. Fellers, M.R. Viant, R.P. McLaughlin, M.G. Brown, R.J. Saykally, *Rev. Sci. Instrum.* 67 (1996) 410.
- [23] W. Sutherland, *Philos. Mag.* 36 (1893) 507.
- [24] R.C. Reid, J.M. Prausnitz, B.E. Poling, *The Properties of Gases, Liquids*, fourth ed., 1987.
- [25] G. Scoles (Ed.), *Atomic and Molecular Beam Methods*, Oxford University Press, Oxford, 1988.
- [26] A.E. Beylich, *Z. Flugwiss, Weltraumforsch* 3 (1979) 48.
- [27] M.J. Zucrow, J.D. Hoffman, *Gas Dynamics*, B1, Wiley, New York, 1976.
- [28] P.J. Linstrom, W.G. Mallard (Eds.), *NIST Chemistry WebBook*, NIST Standard Reference Database Number 69, March 2003.
- [29] X. Tan, F. Salama, *J. Chem. Phys.* 122 (2005) 084318.
- [30] J.M. Weber, K. Hansen, M.W. Ruf, H. Hotop, *Chem. Phys.* 239 (1998) 271.
- [31] S. Matt, B. Dünser, M. Lezius, H. Deutsch, K. Becker, A. Stamatoic, P. Scheier, T.D. Märk, *J. Chem. Phys.* 105 (1996) 1880.